

# Radiation Tolerance of Fully-Depleted P-Channel CCDs Designed for the SNAP Satellite

Kyle Dawson, Chris Bebek, John Emes, Steve Holland, Sharon Jelinsky, Armin Karcher, William Kolbe, Nick Palaio, Natalie Roe, Juhi Saha, Koki Takasaki, and Guobin Wang

**Abstract**—Thick, fully depleted p-channel charge-coupled devices (CCDs) have been developed at the Lawrence Berkeley National Laboratory (LBNL). These CCDs have several advantages over conventional thin, n-channel CCDs, including enhanced quantum efficiency and reduced fringing at near-infrared wavelengths and improved radiation tolerance. Here we report results from the irradiation of CCDs with 12.5 and 55 MeV protons at the LBNL 88-Inch Cyclotron and with 0.1 - 1 MeV electrons at the LBNL  $^{60}\text{Co}$  source. These studies indicate that the LBNL CCDs perform well after irradiation, even in the parameters in which significant degradation is observed in other CCDs: charge transfer efficiency, dark current, and isolated hot pixels. Modeling the radiation exposure over a six-year mission lifetime with no annealing, we expect an increase in dark current of  $20\text{ e}^-/\text{pixel}/\text{hr}$ , and a degradation of charge transfer efficiency in the parallel direction of  $3 \times 10^{-6}$  and  $1 \times 10^{-6}$  in the serial direction. The dark current is observed to improve with an annealing cycle, while the parallel CTE is relatively unaffected and the serial CTE is somewhat degraded. As expected, the radiation tolerance of the p-channel LBNL CCDs is significantly improved over the conventional n-channel CCDs that are currently employed in space-based telescopes such as the Hubble Space Telescope.

**Index Terms**—Astrophysics and Space Instrumentation, Radiation Damage Effects

## I. INTRODUCTION

The SuperNova/Acceleration Probe (SNAP) is a proposed space-based telescope dedicated to the study of dark energy through the observations of Type Ia supernovae (Ia SNe) and a deep, wide area weak lensing survey [1]. From its orbit at the second Earth-Sun Lagrange point (L2), SNAP will carry out two surveys: a deep survey of 7.5 square degree field with repeat visits every four days over a period of 22 months to discover and obtain light curves and spectra of over 2000 Ia supernovae in the redshift range  $0.3 < z < 1.7$ ; and a wide area weak lensing map to study the growth of large scale structure that will cover 1000 square degrees per year to a depth of AB magnitude 28.0 in the optical filters. In an extended 6 year SNAP mission, the weak lensing survey covers 4000 square degrees over the mission lifetime.

The telescope is designed with a 0.7 square degree instrumented field of view divided evenly between 36 CCDs and 36 HgCdTe detectors. The SNAP observing strategy implements a four-point dither pattern with an exposure time of 300 seconds to recover spatial information from the undersampled optics and to reject cosmic rays. The focal plane will be passively

cooled to 140 K. Nine fixed filters cover the wavelength range 400 nm to 1700 nm. With a diffraction limited point spread function (PSF) of 0.1 arcseconds at 800 nm and zodiacal-dominated background, SNAP will have significantly improved resolution and decreased contamination from sky background compared to ground based telescopes.

The SNAP focal plane design uses thick, fully depleted CCDs developed at LBNL [2], [3] for visible to near IR observations in six bandpass filters. In space, these detectors will be exposed to significant radiation, primarily solar protons. In this paper we investigate the effects of six years of radiation at L2 on SNAP CCDs in order to qualify them for use in a space mission. In §II we describe the SNAP CCDs and the specifications for performance. The space environment and expected radiation exposure are discussed in §III. Irradiation using the 88-Inch Cyclotron and the  $^{60}\text{Co}$  source at LBNL is described in §IV and §VI respectively. CCD performance after proton irradiation is reported in §V and after  $^{60}\text{Co}$  irradiation in §VII. Finally, we present an interpretation of the results in the context of the SNAP mission in §VIII and the conclusions in §IX.

## II. CCD REQUIREMENTS

SNAP CCDs have been designed for back-illumination on 200  $\mu\text{m}$  thick, fully-depleted, high-resistivity silicon. A factor of ten increase in thickness over conventional CCDs provides vastly improved sensitivity toward wavelengths of  $1\mu\text{m}$  and negligible fringing effects caused by multiple reflections in the silicon [4], [5]. The CCDs are depleted through application of a substrate bias voltage across the full thickness. The spatial resolution can be improved by increasing the bias voltage up to 200 V [3], with a nominal operating voltage of 100 V for the SNAP mission. The SNAP focal plane will be populated with 36 LBNL CCDs, each having  $3512 \times 3512$   $10.5\mu\text{m}$  pixels.

The objectives of the SNAP experiment are to extract point-source supernovae from diffuse host galaxies and to resolve distant galaxies for weak lensing studies. The specifications for CCD performance are therefore governed by requirements for preservation of the point spread function (PSF), high quantum efficiency (QE), charge transfer efficiency (CTE) and signal-to-noise ratio. In Table I we list the specifications for the SNAP CCDs. As can be seen in the table, each of these requirements has been met in the current design of SNAP style devices before radiation exposure.

CCD performance is expected to degrade in a radiation environment due to bulk damage from non-ionizing energy

The authors are with Lawrence Berkeley National Laboratory, One Cyclotron Rd, Berkeley, CA 94720

Further author information: e-mail kdawson@lbl.gov

TABLE I  
SPECIFICATIONS FOR SNAP CCDS

Quantity	Requirement	Achieved (pre-irradiation)
Wavelength Coverage	400 – 1000 nm	400 – 1000 nm
Quantum Efficiency	> 80% at 600 – 950 nm	> 80% at 600 – 950 nm
Readout Time	> 50% at 1000 nm	> 50% at 1000 nm
Read Noise	30 seconds	30 seconds
Diffusion (RMS)	6 e <sup>-</sup>	4 e <sup>-</sup>
Defect Pixels <sup>a</sup>	6 μm	4 μm
Dark Current <sup>a</sup>	To Be Determined	< 0.1%
Serial CTE <sup>a</sup>	100 e <sup>-</sup> /hr	3 – 4 e <sup>-</sup> /hr
Parallel CTE <sup>a</sup>	To Be Determined	0.999 999
	To Be Determined	0.999 999

<sup>a</sup>expected to deteriorate with irradiation

loss (NIEL) and due to charging of oxide layers from ionizing radiation. This bulk damage manifests itself through decreased charge transfer efficiency, increased dark current, and isolated hot pixels. Current models argue that CTE degradation in conventional n-channel CCDs is caused by traps generated in the formation of phosphorus-vacancy centers [6]. Analysis of dark current in irradiated n-channel devices suggest that an additional damage mechanism is necessary to explain dark current after irradiation. Excess dark current may not be associated with the same impurities as the defects responsible for CTE degradation, and in fact shows a temperature dependence consistent with mid-level traps at slightly higher energies [7]. The mechanism for creating hot pixels is not completely understood and could be explained by several possible radiation-induced defects [8].

The LBNL p-channel CCDs are fabricated on high-resistivity n-type silicon with boron implanted channels. In the p-channel CCDs, divacancy states are expected to be the dominant hole trap [9]–[11]. It has been predicted that divacancy formation in p-channel CCDs is less favorable than phosphorus-vacancy traps in n-channel CCDs [10], and prior studies have shown improved performance after radiation exposure [9], [12], [13].

Ionizing radiation is expected to result in charging of oxide layers, requiring adjustment of pixel gate voltages and output source follower transistor biasing. Significant increases in dark current after ionizing radiation have also been observed in p-channel CCDs [10]. In this work we investigate the effects of both kinds of radiation damage on SNAP CCDs, focusing on generation of dark current, hot pixels, and decrease in charge transfer efficiency.

### III. SPACE ENVIRONMENT AND EXPECTED EXPOSURE

The SNAP satellite will orbit at the L2 Lagrange point, approximately  $1.5 \times 10^6$  km from Earth. At this distance, solar protons dominate the total radiation exposure. To estimate the total exposure at L2, we use the Emission of Solar Protons (ESP) model described in [14] and the Space Environment Information System (SPENVIS) [15]. In SPENVIS, the solar model is simplified as a cycle with seven years at maximum activity with constant exposure and four years at minimum activity with no exposure. The model provides a statistical estimate of the fluence as a function of confidence interval based on data from the past three solar cycles. A simple

shielding model is used in which a spherical aluminum shell surrounds the detectors. The propagation of particles through the shielding is also simplified; showers and secondary particles are not modeled. With these simplifications, we make a first-order estimate of the effects of radiation on the SNAP visible detectors. A more detailed Monte Carlo simulation of the propagation of particles through the structures of the satellite will be performed at a later date.

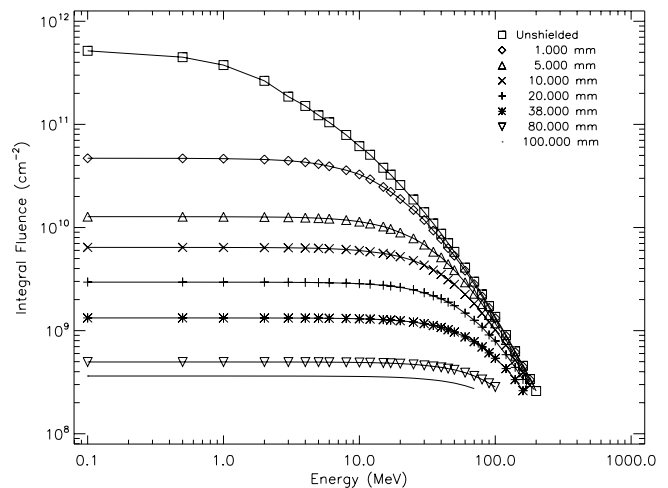


Fig. 1. Spectrum of incident particles for various shielding thicknesses (Al equivalent). Results indicate 95% upper limits assuming a six year mission with launch date January 1, 2014. A shielding thickness of  $\sim 38$  mm is the average amount of shielding of the SNAP focal plane.

Assuming a six year extended mission with a January 1, 2014 launch date, we estimate the accumulated radiation exposure for the SNAP CCDs at the 95% confidence level. Figure 1 shows the spectrum of protons incident on the detectors for various shield thicknesses predicted by ESP and SPENVIS. Similarly, Figure 2 reports the total expected displacement damage dose due to NIEL as a function of shield thickness.

Analysis of the satellite mechanical structure shows the detector shielding thickness varies by almost a full order of magnitude over the full range of angles of incidence. The distribution of the material surrounding the focal plane over  $4\pi$  is shown in Figure 3. The present satellite design provides an average shielding equivalent to about 47 mm of Al shielding around the focal plane, with a minimum of 9 mm of Al equivalent over a small fraction of the solid

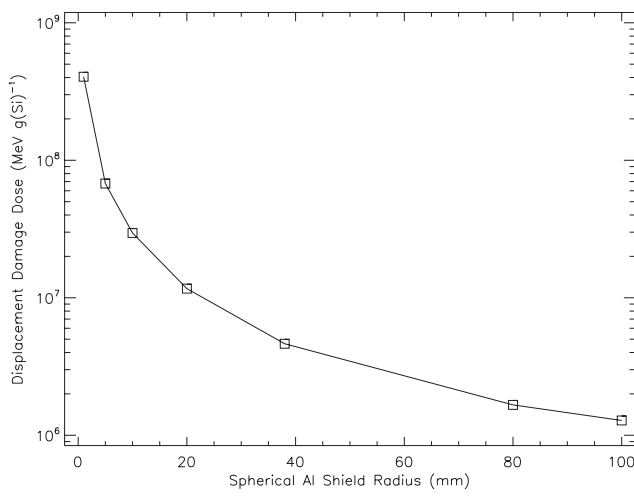


Fig. 2. Displacement damage dose as a function of shielding thickness. Results indicate 95% upper limits assuming a six year mission with launch date January 1, 2014. For comparison, the average amount of shielding surrounding the SNAP focal plane is equivalent to 47 mm of aluminum.

angle. The SNAP satellite has not yet been fully optimized for radiation shielding, and future modifications can provide additional shielding in the thinnest regions, so our current estimates may be considered conservative.

We have computed the average displacement damage dose at the SNAP focal plane by folding the expected exposure at L2 as a function of shield thickness with the distribution of shielding thickness in the current SNAP design. We find an integrated displacement damage dose of  $6.6 \times 10^6$  MeV/g (Si) over the  $4\pi$  solid angle. Assuming a NIEL factor of  $8.9 \times 10^{-3}$  Mev/g/cm<sup>2</sup> for 12.5 MeV protons [16], this is equivalent to a fluence of  $7.4 \times 10^8$  12.5 MeV protons/cm<sup>2</sup>. We report results of the radiation tolerance of the SNAP CCDs treating this fluence as a “nominal” value that will be experienced by the SNAP CCDs at 95% CL after six years at L2.

#### IV. IRRADIATION AT THE LBNL 88-INCH CYCLOTRON

Nine CCDs were characterized before irradiation, with performance very similar to that described in Table I. Charge transfer efficiency (CTE) was measured using the <sup>55</sup>Fe 5.9 keV line [13] for both parallel and serial transfers. Gain conversion from ADC count (ADU) to e<sup>-</sup> was also determined using <sup>55</sup>Fe images. Dark current was determined from the mean signal over the whole device relative to the overscan,

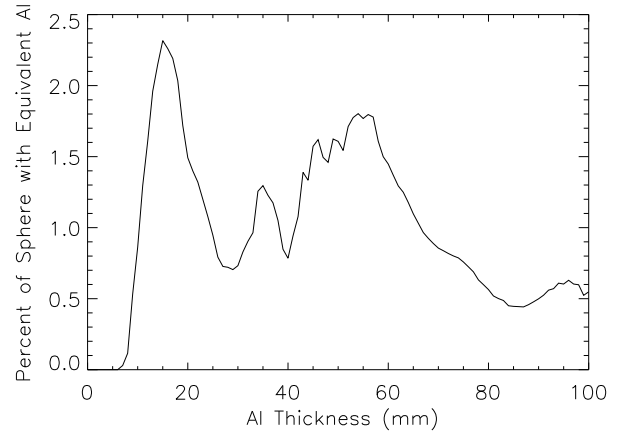


Fig. 3. Distribution of the shield thickness surrounding the SNAP focal plane over the full  $4\pi$  solid angle.

in 10 minute dark exposures, after removal of  $3\sigma$  outliers to account for cosmic ray contamination. Ten dark images were taken successively and median-combined to generate a high signal-to-noise dark image, free of cosmic rays and terrestrial background radiation. Residual hot pixels, caused by a clustering of mid-level traps for example [17], [18], were identified as high significance peaks in this median-combined image. Very rarely was even a single individual hot pixel identified in a dark image at 133 K. More common were manufacturing defects, the occasional hot column caused by a minor clock short or back-side defect. For a more detailed account of clock shorts and back-side defects, see [19].

To simulate radiation exposure in the space environment, CCDs 1-8 listed in Table II were exposed at the LBNL 88-Inch Cyclotron for irradiation to 12.5 and 55 MeV protons. For convenience, most of the radiation exposures were carried out at room temperature on CCDs with all of the inputs shorted together and no bias voltages present. The proton fluence was continuously monitored during irradiation using standard ion chamber dosimetry.

To check whether warm irradiation gives the same results as irradiation at cryogenic temperatures, a full-size SNAP CCD was irradiated in a dewar at 133 K at nominal bias and clocking voltages and continuous readout at 70 kHz during the exposure. A brass shield inside the dewar could be moved into three different positions, resulting in exposures to three different regions of the CCD. The cold-irradiated CCDs

TABLE II

LIST OF IRRADIATED CCDS. BI REFERS TO BACK-ILLUMINATED DEVICES WHILE FI REFERS TO FRONT-ILLUMINATED DEVICES.

Device #	Format	Radiation	Energy	Warm/Cold	Fluence
1	3512 × 3512 pixels, FI	proton	55 MeV	warm	$5 \times 10^9, 1 \times 10^{10}, 5 \times 10^{10}, 1 \times 10^{11}$ protons/cm <sup>2</sup>
2	3512 × 3512 pixels, FI	proton	12.5 MeV	warm	$5 \times 10^9, 1 \times 10^{10}, 5 \times 10^{10}, 1 \times 10^{11}$ protons/cm <sup>2</sup>
3	3512 × 3512 pixels, BI	proton	12.5 MeV	warm	$5 \times 10^9, 1 \times 10^{10}, 5 \times 10^{10}, 1 \times 10^{11}$ protons/cm <sup>2</sup>
4	3512 × 3512 pixels, FI	proton	12.5 MeV	cold	$5 \times 10^9, 1 \times 10^{10}, 2 \times 10^{10}$ protons/cm <sup>2</sup>
5	1700 × 1836 pixels, FI	proton	12.5 MeV	warm	$5 \times 10^9$ protons/cm <sup>2</sup>
6	1700 × 1836 pixels, FI	proton	12.5 MeV	warm	$1 \times 10^{10}$ protons/cm <sup>2</sup>
7	1700 × 1836 pixels, FI	proton	12.5 MeV	warm	$5 \times 10^{10}$ protons/cm <sup>2</sup>
8	1700 × 1836 pixels, FI	proton	12.5 MeV	warm	$1 \times 10^{11}$ protons/cm <sup>2</sup>
9	3512 × 3512 pixels, FI	electron	0.1 - 1.0 MeV	cold	1.2 krad

allowed us to study the time evolution of the dark current, and the rate at which hot pixels were generated. In the warm-irradiated devices, both dark current and hot pixels quickly annealed at room temperature, so only the cold-irradiated CCDs could give an indication of the long-term effects. In addition, we carried out controlled periods of warming on the cold-irradiated devices to study the effects of annealing.

## V. RESULTS OF PROTON IRRADIATION

Measurements on the warm-irradiated devices were made beginning four weeks after irradiation to allow the dark current to decay to a low level. Otherwise, the abnormally high dark current would mitigate the effects of degraded CTE by filling the defects created during irradiation. After this cooling period, the CCDs were again characterized as described above to determine of the CTE as a function of fluence and energy.

For CTE measurements, the  $^{55}\text{Fe}$  linear density was approximately one x-ray per 80 pixels for devices 1-3 and devices 5-8. The density was approximately one x-ray per 270 pixels for devices 4 and 9. All CTE measurements were carried out at a temperature of 133 K at a pixel readout rate of 70 kHz. Because of the delay between parallel transfers as each row is serially read one pixel at a time, charge is transferred about three orders of magnitude faster in the serial (line) direction than in the direction of parallel (row) transfer. The traps are most efficient when the transfer rate is comparable to the de-trapping time constant.

The cold, proton-irradiated device 4 was maintained at 133 K for 54 days following irradiation. Dark and  $^{55}\text{Fe}$  images were collected on a regular basis, beginning three days after the irradiation. The primary purpose of the cold-irradiation and analysis was to determine the evolution of CTE, dark current, and isolated hot pixels at normal operating conditions over an extended period. After 54 days, the device was allowed to anneal to room temperature for a period of 12 hours and then cooled back down to 133 K for CTE and dark current measurements. Measurements were again taken daily for another seven weeks starting six days after the anneal was initiated. Comparison of the CCD performance before and after warming provide data on the effects of annealing, an analysis not possible with the warm-irradiated CCDs.

### A. Comparison of CTE on front- and back-illuminated CCDs

Most of the irradiated devices were  $650\ \mu\text{m}$  thick, front-illuminated (FI) CCDs. Front-illumination refers to the light impinging on the front, or patterned, side of the CCD (CCDs used for astronomy are always back-illuminated for improved quantum efficiency). The FI devices lend themselves to CTE testing since  $^{55}\text{Fe}$  x-rays are deposited directly on the pixels, without the lateral charge diffusion that occurs in back-illuminated (BI) devices. One  $200\ \mu\text{m}$  thick, BI SNAP device (device 3) was irradiated for comparison. CTE was measured on the irradiated BI device using the extended pixel edge response (EPER) and first pixel response (FPR) techniques [23], instead of x-rays. A detailed comparison of the BI device 3 with FI device 2 with EPER and FPR showed a similar degradation of CTE with fluence. From this we conclude that

the use of  $650\ \mu\text{m}$  thick, front-illuminated devices for the study of CTE degradation with fluence is a reasonable substitution for  $200\ \mu\text{m}$  thick, back-illuminated devices.

### B. Energy Dependence of CTE Degradation

To test the validity of the NIEL scaling for CTE degradation, a SNAP CCD irradiated at 55 MeV was compared to a SNAP CCD irradiated at 12.5 MeV (devices 1 and 2 in Table II). If CTE degradation scales with NIEL then the damage factor, defined as  $\text{CTI}/\text{fluence}/\text{NIEL}$  in units of  $\text{CTI}/\text{MeV}\cdot\text{N}_p$  for a fixed material, should be similar for both energies. As can be seen in Table III, the damage factor describing serial charge transfer inefficiency ( $\text{CTI}=1-\text{CTE}$ ) is nearly identical for both energies, well within the uncertainty of the measurement. The damage factor was observed to be 15% larger in parallel CTE in the case of the 55 MeV irradiation, a relatively minor difference of  $1.5\ \sigma$ .

TABLE III  
CTE DEGRADATION IN SI AT 12.5 MEV AND 55 MEV FOR A FLUENCE OF  $1 \times 10^{11}$  PROTONS/CM<sup>2</sup>.

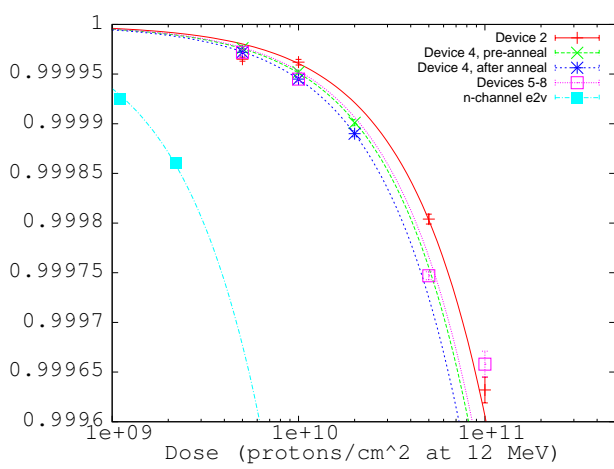
Energy (MeV)	Transfer Direction	CTI $\times 10^{-4}$	NIEL $\text{MeV}\cdot\text{cm}^2/\text{g}$ $\times 10^{-3}$	Damage Factor $\text{CTI}/\text{fluence}/\text{NIEL}$ $\times 10^{-13}$
12.5	parallel	$3.9 \pm 0.3$	8.9	$4.4 \pm 0.3$
55	parallel	$2.1 \pm 0.2$	4.1	$5.1 \pm 0.5$
12.5	serial	$3.1 \pm 0.4$	8.9	$3.5 \pm 0.4$
55	serial	$1.5 \pm 0.2$	4.1	$3.7 \pm 0.5$

### C. Scaling of CTE with Fluence

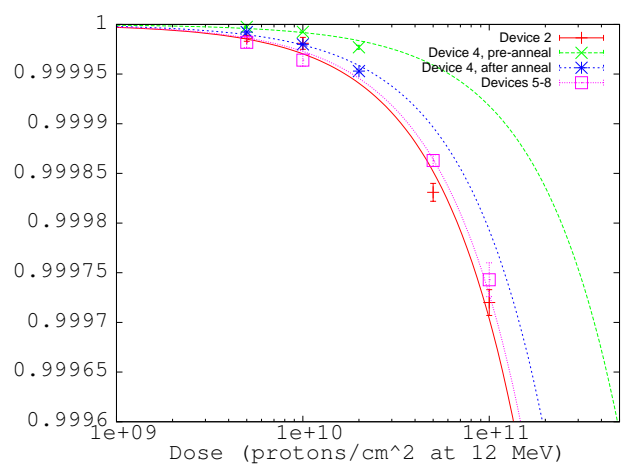
The irradiated devices included both full-size  $3512 \times 3512$  pixel SNAP CCDs and "mini-SNAP" CCDs of smaller format  $1700 \times 1836$  pixels but of otherwise identical design. With the use of a brass shield, the four quadrants of the full-size SNAP CCDs were individually exposed to  $5 \times 10^9$ ,  $1 \times 10^{10}$ ,  $5 \times 10^{10}$  and  $1 \times 10^{11}$  protons/cm<sup>2</sup>; the mini-SNAP devices each received a single uniform exposure. Comparison of the results for device 2 with devices 5, 6, 7, and 8 (Figures 4(a) and 4(b)) indicates that the radiation damage effects observed on the mini-SNAP CCDs were consistent with those observed on the full-size SNAP CCDs, thus validating the use of small-format devices of otherwise identical design for radiation studies.

The CTE of devices 2, 4, and 5-8 was analyzed and compared over the full range of exposure levels. Results of the degradation of parallel CTE are shown in Figure 4(a). There is a slight difference in the parallel CTE among the different radiation exposure conditions. This may be due to differences in the level of dark current, which can account for changes on the order of a few  $\times 10^{-5}$  in CTE at a fluence of  $2 \times 10^{10}$  protons/cm<sup>2</sup>, as discussed in §V-E. The background from dark current in the cold-irradiated device before the anneal was typically  $\sim 10 - 40\ e^-/\text{pix}$ , while the background in the warm-irradiated devices and in device 4 after annealing was typically  $\sim 2 - 8\ e^-/\text{pix}$ .

For comparison, we also include the results of CTE testing on conventional n-channel CCDs from e2v [12] in Figure 4(a). The n-channel CCDs are intended to be used in the Wide



(a) Parallel CTE as a function of fluence



(b) Serial CTE as a function of fluence

Fig. 4. a) Parallel CTE as a function of fluence for SNAP CCDs and n-channel e2v CCD similar to that used in ACS on HST with model fits. The n-channel e2v CCD was tested at a temperature of 190 K. b) Serial CTE as a function of fluence for SNAP CCDs with model fits. The x-axis in both figures is shown in log-scale to provide the dynamic range required to identify individual data points and best fit models. Each set of data points is fit assuming a simple two parameter linear model.

Field Camera 3 (WFC3) on the Hubble Space Telescope (HST) and were irradiated using 63 MeV protons with a fluence of  $2.5 \times 10^9$  protons/cm<sup>2</sup> and  $5 \times 10^9$  protons/cm<sup>2</sup>, equivalent to 2.5 and 5.0 years in the HST orbit. Assuming a NIEL factor of  $3.7 \times 10^{-3}$  MeV-cm<sup>2</sup>/g (Si) for 63 MeV protons [16], the equivalent fluence at 12.5 MeV is  $1.04 \times 10^9$  protons/cm<sup>2</sup> and  $2.08 \times 10^9$  protons/cm<sup>2</sup>. CTE measurements were made at 190 K which will be the operating temperature on HST. It has been reported that CTE performance in n-channel devices can improve by as much as a factor of ten when cooled from 190 K to 160 K [20], however we report the results as a comparison of the expected performance of WFC3 and SNAP in nominal operating conditions.

Serial CTE vs fluence is shown in Figure 4(b). As can be seen in the figure, the warm-up to room temperature resulted in a decrease in the serial CTE, an effect referred to as "reverse annealing." We also observe a significantly worse serial CTE performance in the warm-irradiated CCDs, compared to the cold-irradiated device both before and after annealing. It has been demonstrated that irradiation produces only negligible degradation of serial CTE in the n-channel e2v devices [21] and results are not included here.

#### D. Effect of Annealing on CTE

Reverse annealing has also been observed in the n-channel CCDs used in the Chandra telescope. Following that analysis [22], we analyze the de-trapping time constants before and after annealing by computing the average signal in the pixels following the main charge packet in the <sup>55</sup>Fe images from the cold, proton-irradiated device 4.

Each x-ray event is identified, centroided in  $3 \times 3$  pixel box, and included in the analysis if the center position is within 0.1 pixels of the center pixel. This selection rejects events in which the x-ray is deposited near a pixel boundary. The charge is counted in each trailing pixel as a fraction of the charge in the primary charge packet for the parallel or serial directions.

We then divide the trail of charge of each event by the total number of transfers and average the results. In other words, the averaged trails represent the fraction of charge left behind the primary charge packet for a single transfer. The results before and after the anneal for parallel and serial clocking are found in Figure 5.

The trailing charge is well fit by a two term exponential of the form

$$Q(t) = A_1 e^{-t/\tau_1} + A_2 e^{-t/\tau_2} \quad (1)$$

where  $Q(t)$  is the number of counts following the main charge packet as a function of time. The best fits are plotted in Figure 5, and the parameters are reported in Table IV.

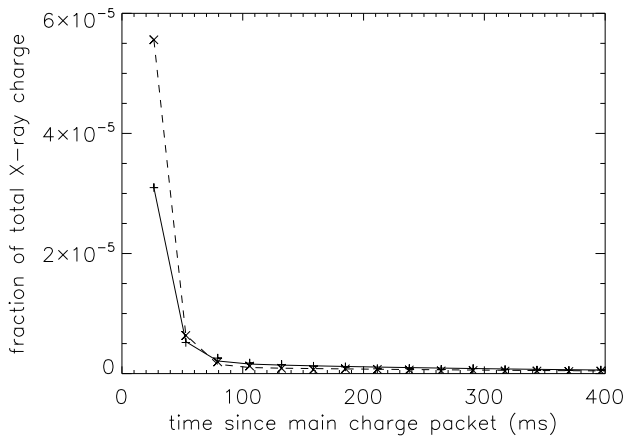
One can compute the amount of charge described by both terms of the exponential decay by simply integrating the best fit curve to infinity. The ratio of the integrals

$$R = \frac{\int_0^\infty A_1 e^{-t/\tau_1} dt}{\int_0^\infty (A_1 e^{-t/\tau_1} + A_2 e^{-t/\tau_2}) dt} \quad (2)$$

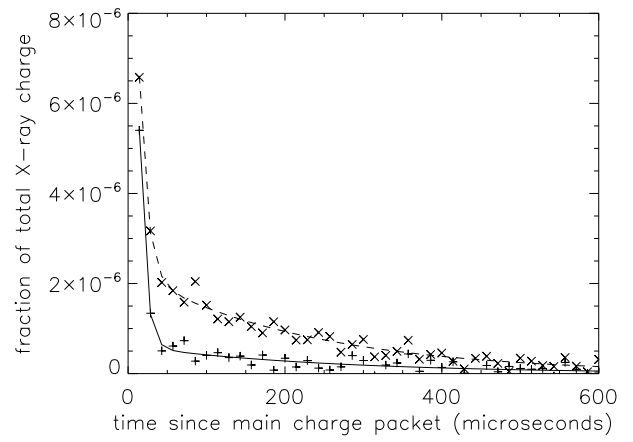
determines the fraction of charge that is contained in the fast decay term compared to the total charge contained in the trails.

For the parallel CTE, most of the trailing charge is contained in the fast decay term: 77% before the anneal, and 92% after the anneal. For the serial CTE, however, a significant difference is observed between the pre-anneal trailing charge and the post-anneal trailing charge. Before the anneal, 65% of the trailing charge is contained in the fast decay term. After the anneal, the longer decay term dominates, with only 29% of the charge being contained in the fast decay term.

The significant change in the characteristics of the serial trailing charge indicates a transition in the trap population caused by the anneal. Previous studies indicate that divacancies are the traps primarily responsible for CTE degradation in LBNL CCDs, with carbon interstitials and carbon-oxygen traps playing a less significant role [13]. It is possible that a population of relatively benign lattice vacancies is generated



(a) Parallel trails



(b) Serial trails

Fig. 5. a) Distribution of trailing charge in the parallel direction. Counts are normalized to the number of counts measured in lead pixel, divided by the number of parallel transfers. b) Distribution of trailing charge in the serial direction. Counts are normalized to the number of counts measured in the lead pixel divided by the number of serial transfers. In both cases, the solid curve and '+' symbols represent results before the anneal. The dashed curve and 'x' symbol represent results following the anneal. A data point is taken for every pixel following the main charge.

TABLE IV  
CHARACTERIZATION OF TRAILING CHARGE

Measurement	$A_1$	$\tau_1$ (s)	$A_2$	$\tau_2$ (s)
Parallel - pre-anneal	$(1.75 \pm 0.04) \times 10^{-4}$	$(1.40 \pm 0.02) \times 10^{-2}$	$(1.84 \pm 0.06) \times 10^{-6}$	$(4.06 \pm 0.20) \times 10^{-1}$
Parallel - post-anneal	$(5.02 \pm 0.06) \times 10^{-4}$	$(1.16 \pm 0.01) \times 10^{-2}$	$(1.28 \pm 0.04) \times 10^{-6}$	$(3.70 \pm 0.14) \times 10^{-1}$
Serial - pre-anneal	$(3.42 \pm 0.38) \times 10^{-5}$	$(7.72 \pm 0.44) \times 10^{-6}$	$(0.64 \pm 0.06) \times 10^{-6}$	$(2.23 \pm 0.26) \times 10^{-4}$
Serial - post-anneal	$(2.21 \pm 0.14) \times 10^{-5}$	$(9.30 \pm 0.34) \times 10^{-6}$	$(2.22 \pm 0.04) \times 10^{-6}$	$(2.25 \pm 0.05) \times 10^{-4}$

during the initial cold irradiation, and remains stable at low operating temperatures. If this is the case, it appears that this population becomes mobile at room temperature, possibly forming more stable, and more efficient divacancy traps during the annealing process. A full diagnosis of the effects of the reverse anneal requires measurements of pocket-pumping [23] and CTE as a function of temperature to constrain the trap properties before and after the anneal. Such an analysis is beyond the scope of this paper and will be addressed in future publications.

### E. Effects of Trap-Filling on CTE Performance

It is well known that trap-filling by background sky and neighboring objects can mitigate the effects of CTE degradation [23]. In this section we describe an effort to model the dependence of CTE in SNAP CCDs on the background sky level and the density of  $^{55}\text{Fe}$  events.

Device 4 was imaged with varying exposure times to control the level of dark current and varying shutter times to control the density of  $^{55}\text{Fe}$  events. We took several sets of data, covering a factor of 40 in both the range of background sky values and  $^{55}\text{Fe}$  densities, both before and after annealing.

Sky dependent corrections to CTI have been modeled for observations with the Advanced Camera for Surveys (ACS) [24]. In the corrections to account for trap-filling on the ACS on HST, it was assumed that the CTI dependence on both the sky background and the source intensity is described by a power law. Such an assumption produces a singularity in the limit of low sky background or low source intensity. The data is quite noisy in both the ACS analysis and in this analysis, and it is difficult to determine which analytic function best describes the data. We avoid the singularities introduced by a power law and simply assume that sky level and source density affect the CTI independently. We fit the data with an exponential law of the form

$$CTI(s, \rho) = A_1 e^{-s/s_0} + A_2 e^{-\rho/\rho_0} + C \quad (3)$$

where  $s$  represents the sky level in units of  $e^-/\text{pixel}$ ,  $\rho$  is the density of x-ray events in units of events/pixel, and  $A_1$ ,  $A_2$ ,  $s_0$ ,  $\rho_0$ , and  $C$  are the parameters to be fit. Parameters are determined by a fit to the pre-anneal data in the quadrant that received an exposure of  $2 \times 10^{10}$  protons/cm<sup>2</sup>. The dark current in the post-anneal data was very low and the data were not sufficient to constrain the model.

TABLE V  
BEST FIT PARAMETERS TO TRAP-FILLING MODEL

Measurement	$A_1$	$s_0$ ( $e^-/\text{pixel}$ )	$A_2$	$\rho_0$ (events/pixel)	$C$
Parallel	$(5.6 \pm 1.3) \times 10^{-5}$	$14.6 \pm 3.1$	$(4.1 \pm 0.6) \times 10^{-5}$	$(1.2 \pm 0.4) \times 10^{-2}$	$(5.0 \pm 1) \times 10^{-5}$
Serial	$(2.7 \pm 1.7) \times 10^{-6}$	$53 \pm 99$	$(1.7 \pm 1.2) \times 10^{-5}$	$(1.6 \pm 2.2) \times 10^{-2}$	$(9.0 \pm 14) \times 10^{-6}$

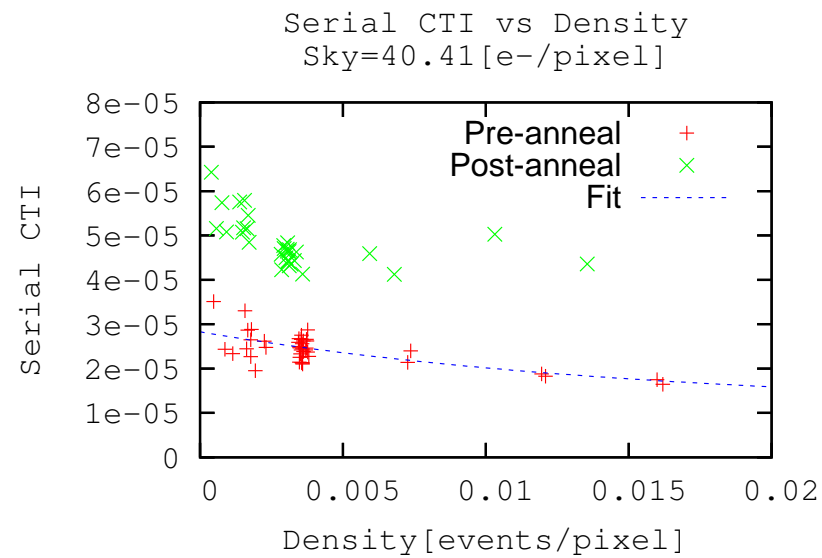
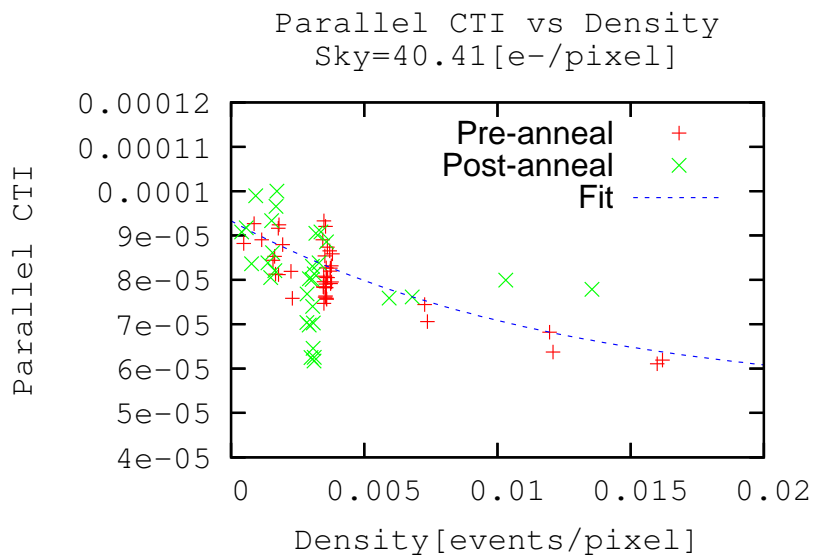
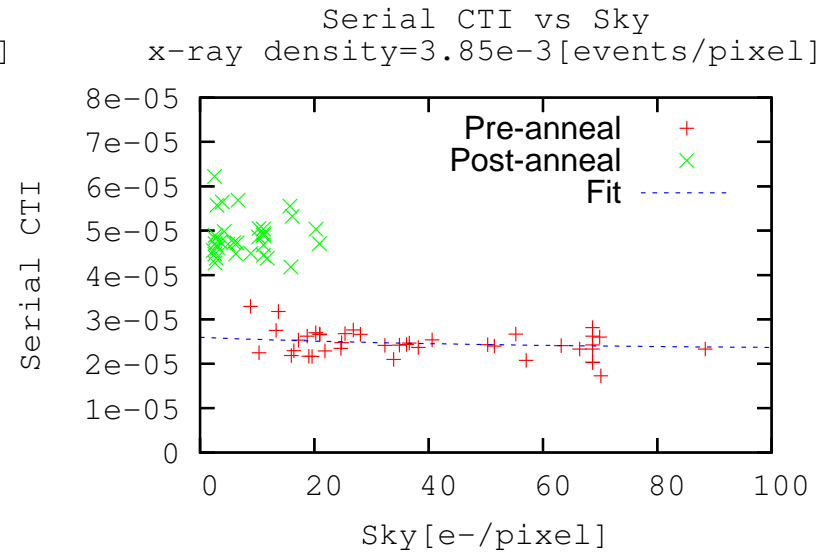
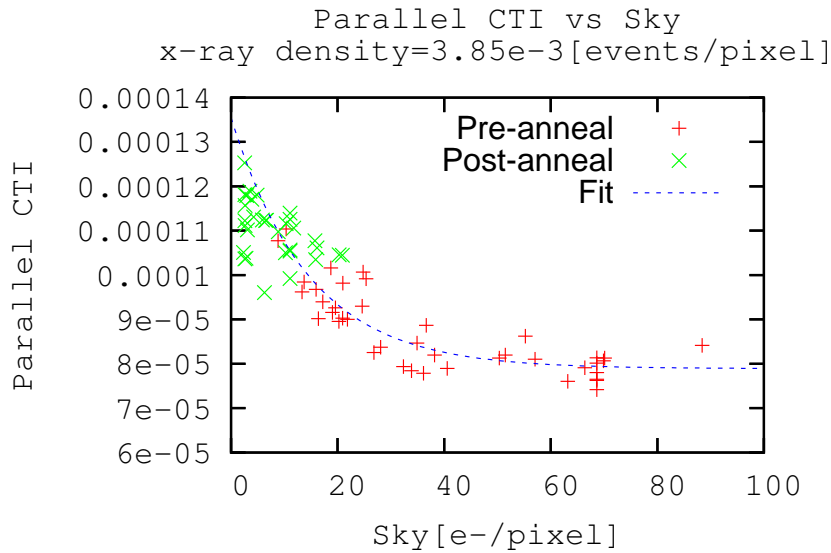


Fig. 6. Dependence of CTI on sky level and density of x-ray events for both the parallel and serial CTI after exposure to  $2 \times 10^{10}$  protons/cm<sup>2</sup>. Upper left: Parallel CTI vs sky level. Upper right: Serial CTI vs sky level. CTI is normalized to x-ray density of  $3.85 \times 10^{-3}$  events/pixel. Lower left: Parallel CTI vs x-ray density. Lower right: Serial CTI vs x-ray density. CTI is normalized to sky level of 40.41 e<sup>-</sup>/pixel.

The best fit parameters that describe the CTI as a function of background level and x-ray density are found in Table V. The CTI data as a function of sky level and density are reported along with the best fit model in Figure 6. In the two upper tiles of the figure, CTI is plotted versus sky level after normalization to  $3.85 \times 10^{-3}$  x-ray events per pixel using the best fit parameters. In the two lower tiles, CTI is plotted versus x-ray density after normalization to a sky level of  $40.41 \text{ e}^-/\text{pixel}$ . For parallel CTI, both the pre-anneal and post-anneal data are well described by the same set of parameters. It is evident from the figure that the serial CTI after the anneal follows a significantly different relationship than the pre-anneal data, another indication of a transition in the trap population caused by the anneal cycle. Also demonstrated in Figure 6 is that the mitigation of CTE from the background sky and x-ray density is more pronounced in the parallel transfer direction than in the serial transfer direction. The biggest improvement appears to come from an increased sky background, decreasing the parallel CTI from  $1.3 \times 10^{-4}$  at zero background to  $8.0 \times 10^{-5}$  at a background of  $40\text{--}100 \text{ e}^-/\text{pixel}$  at the fixed x-ray density of  $3.85 \times 10^{-3}$  events per pixel.

### F. Generation of Hot Pixels

Median-stacked, cosmic ray-cleaned dark images from before and after irradiation were compared in the quadrant which was exposed to a fluence of  $2 \times 10^{10}$  protons/cm<sup>2</sup> in the cold-irradiated SNAP CCD (device 4). Using a simple scheme to subtract the pre-irradiation image from the post-irradiation image, a map was generated to identify residuals produced as a result of the irradiation. Hot isolated pixels in this residual map represent spikes in dark current which will be flagged in a bad pixel map for science images. Hot pixels are located and counted by identifying pixels that lie a certain threshold above the mean background level. The pre-anneal number density of these hot pixels as a function of time and threshold is shown in Figure 7.

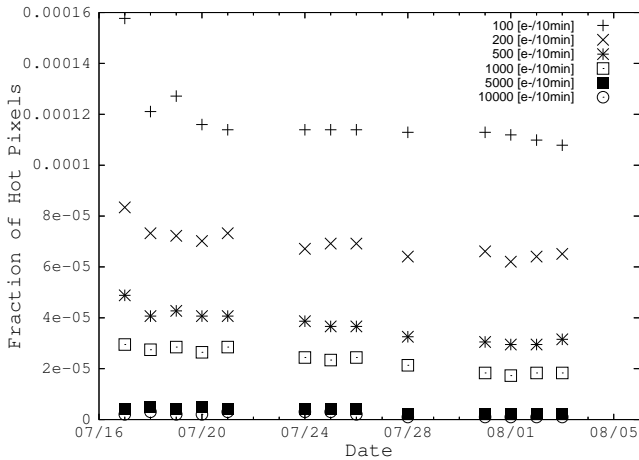


Fig. 7. Isolated hot pixels after irradiation with  $2 \times 10^{10}$  protons/cm<sup>2</sup>.

With a threshold of  $100 \text{ e}^-$  in a ten minute exposure, the density of hot pixels is  $1.13 \times 10^{-4}$  for a fluence of  $2 \times 10^{10}$  protons/cm<sup>2</sup>. The density of hot pixels is  $3.1 \times 10^{-5}$  with a threshold of  $500 \text{ e}^-$  in a ten minute exposure. After

the 12 hour anneal to room temperature described in §V, the already negligible density of hot pixels drops dramatically.

A similar experiment was conducted using n-channel CCDs designed by e2v for WFC3. The e2v CCDs were exposed to 63 MeV protons at a total fluence of  $2.5 \times 10^9$  protons/cm<sup>2</sup>, equivalent to an exposure at 12.5 MeV of  $1.04 \times 10^9$  protons/cm<sup>2</sup>. The device was stored at room temperature for 60 days after exposure before cooling down to normal operating conditions for additional measurements. After the anneal, a fraction of  $2.5 \times 10^{-3}$  hot pixels were detected at a threshold of  $26 \text{ e}^-/10 \text{ min}$  [25]. Applying this threshold to the LBNL data, and scaling the result to the same fluence, we find a fraction of  $2.0 \times 10^{-5}$  hot pixels before the anneal and  $1.3 \times 10^{-6}$  hot pixels after the anneal in the SNAP device.

The improvement by over two orders of magnitude in the rate of hot pixels for the LBNL CCDs relative to the e2v CCDs is at least in part due to the different operating temperatures for the SNAP ( $-133 \text{ C}$ ) and WFC3 ( $-83 \text{ C}$ ) focal planes. The rate of hot pixels in the e2v CCDs was observed to decline by two orders of magnitude as operating temperature was reduced from  $-65 \text{ C}$  to  $-90 \text{ C}$ . The hot pixel rate in LBNL CCDs has not been studied at the higher temperature of the WFC3 instrument.

### G. Evolution of Dark Current

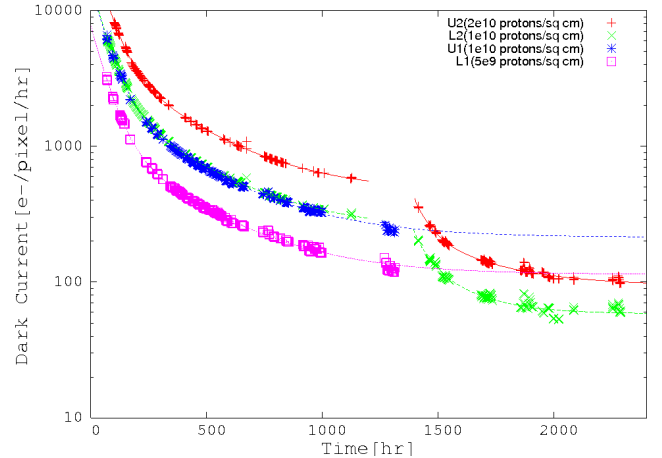


Fig. 8. Evolution of dark current in cold-irradiated device with anneal at 1300 hours. No data was taken between 1300 hours and 1450 hours and no model is fit in this region for the quadrants labeled U2 and L2. After the anneal, the data from these two quadrants was fit by a second two-term exponential. To illustrate the effects of the anneal, the pre-anneal data from quadrants L1 and U1 is extrapolated to 2500 hours.

The level of dark current ( $DC$ ) for device 4 as a function of time can be found in Figure 8. Dark current was measured as described in §IV and no large-scale structure was observed in the dark current generated after irradiation. The evolution of dark current is well described by a two term exponential decay,

$$DC = A_0 e^{-t/t_0} + A_1 e^{-t/t_1} + C \quad (4)$$

where  $A_0$  and  $A_1$  describe the amplitude of the two exponential terms, in units of  $\text{e}^-/\text{pixel}/\text{hr}$ , and  $t_0$  and  $t_1$  are the

corresponding time constants. The model is fit to the data, and best-fit parameters can be found in Table VI. The curve described by the best-fit model for each fluence is found in Figure 8. Examination of the best fit parameters indicate that the dark current scales roughly with fluence before the anneal and that the time constants are not fluence dependent. It is also evident from Table VI that the decay time constants are short compared to the mission lifetime. A room temperature anneal appears to initiate a second decay in the dark current with time constants similar to those observed immediately following the exposure.

## VI. IRRADIATION WITH THE LBNL $^{60}\text{Co}$ SOURCE

In order to separate the effects of ionizing radiation damage from the effects of NIEL radiation damage, another SNAP CCD (device 9 in Table II) was irradiated at the  $^{60}\text{Co}$  source at LBNL. The CCD was mounted in a dewar with an Al window of thickness 0.75 mm in place of the usual glass window. 2 mm of Pb shielding was placed in between the dewar and the  $^{60}\text{Co}$  source. The device was powered and irradiated for 30 minutes at a temperature of 133 K.

The primary mechanism for radiation damage in this experiment is energy deposition from ionizing electrons in the 0.1 - 1 MeV range. Electrons are excited from the Pb shielding through Compton scattering of 1.1 and 1.3 MeV  $^{60}\text{Co}$  photons. The Al window at the dewar opening was designed to prevent the generation of excess electron-hole pairs from remaining low energy photons. An estimate of the total ionizing dose of 1.2 krad was determined through Monte Carlo simulations of the propagation of photons and electrons through the Pb and Al shielding. The estimate of the Monte Carlo simulations was confirmed within 10% using thermoluminescent dosimeters (TLDs) placed at various locations between the CCD and the  $^{60}\text{Co}$  source. After irradiation, measurements of dark current were obtained for comparison to the cold-irradiated device described in §V-G. The  $^{60}\text{Co}$ -irradiated device was maintained at 133 K for five days following irradiation. Dark images were collected several times a day, starting 30 minutes after irradiation. No measurable degradation of CTE was observed in the CCD irradiated at the  $^{60}\text{Co}$  source.

## VII. RESULTS OF $^{60}\text{Co}$ IRRADIATION

We observed the time evolution of dark current in the  $^{60}\text{Co}$ -irradiated device for comparison to the proton-irradiated device. The highest fluence received by the cold, proton-irradiated CCD (device 4) was  $2 \times 10^{10}$  protons/cm<sup>2</sup> at

12.5 MeV, corresponding to an ionizing dose of 9.38 krad. As mentioned in §VI, the total ionizing dose in the  $^{60}\text{Co}$  irradiation was 1.2 krad. Assuming the damage scales linearly with ionizing dose, the dark current measured in device 9 was rescaled to an ionizing dose of 9.38 krad for direct comparison to the proton-irradiation. This rescaling equates to a factor of  $9.38/1.2 = 7.8$  increase in the dark current measured in the  $^{60}\text{Co}$  irradiation. The results compared to the proton-irradiated CCD are found in Figure 9. A two term exponential model describing the time evolution of dark current in the  $^{60}\text{Co}$  irradiated CCD is fit to the data. The best fit parameters are found in Table VI.

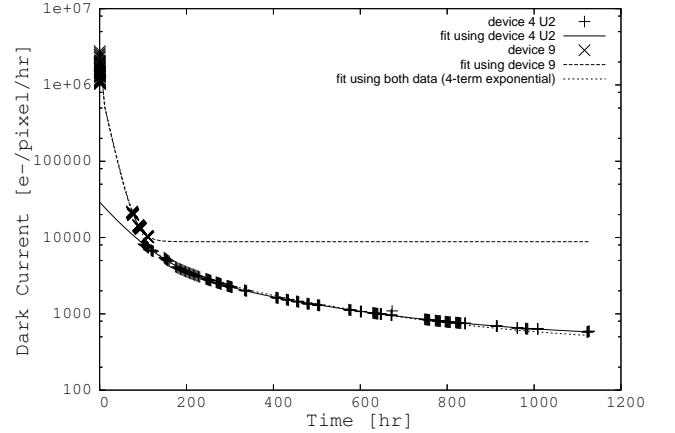


Fig. 9. Evolution of dark current in proton irradiated CCD (device 4) compared to  $^{60}\text{Co}$  irradiated CCD (device 9). Measurements were done for both devices at a temperature of 133 K.

The time frame of the measurements for the  $^{60}\text{Co}$  radiation is quite different from that of the proton-irradiation measurements. There is almost no overlap between the regimes probed in the  $^{60}\text{Co}$  irradiation, where no data exists after 100 hours, and in the proton-irradiation where no data exists before 100 hours. The data from the  $^{60}\text{Co}$  irradiation only appears to be sensitive to time constants shorter than approximately 20 hours while the data from the proton-irradiation appears to be sensitive to time constants on the order of a few days or longer. Nevertheless, a comparison of the decay amplitudes found in Figure 9 suggests that the dark current evolution from ionizing irradiation is quite similar to the evolution of dark current in proton-radiation. Time constants of 0.32 hours and 17.2 hours describe the  $^{60}\text{Co}$  dark current in the 100 hours immediately following irradiation and time constants of 61.5 hours and 311 hours describe the proton-irradiation dark current at somewhat

TABLE VI  
PARAMETERS DESCRIBING EVOLUTION OF DARK CURRENT

Fluence	$A_0$ (e <sup>-</sup> /px/hr)	$t_0$ (hr)	$A_1$ (e <sup>-</sup> /px/hr)	$t_1$ (hr)	C (e <sup>-</sup> /px/hr)
Before Room Temperature Anneal					
$5 \times 10^9$	$6500 \pm 40.7$	$61.9 \pm 0.7$	$1050 \pm 27.8$	$331 \pm 9.5$	$113 \pm 4.1$
$1 \times 10^{10}$	$12900 \pm 136$	$63.4 \pm 1.2$	$2100 \pm 108$	$328 \pm 19.5$	$228 \pm 20.0$
$2 \times 10^{10}$	$24300 \pm 470$	$61.5 \pm 1.3$	$4200 \pm 156$	$311 \pm 12.1$	$466 \pm 20.5$
$^{60}\text{Co}$	$(3.4 \pm 0.24) \times 10^6$	$0.32 \pm 0.04$	$(1.0 \pm 0.08) \times 10^6$	$17.2 \pm 1.6$	$(8.8 \pm 2.7) \times 10^3$
Following Room Temperature Anneal					
$1 \times 10^{10}$	$398 \pm 90$	$52.8 \pm 15$	$142 \pm 47$	$194 \pm 37$	$58 \pm 3$
$2 \times 10^{10}$	$730 \pm 44$	$59.6 \pm 4.9$	$178 \pm 21$	$288 \pm 32$	$94 \pm 2.5$

later times (columns 3 and 5 in Table VI). We find the two data sets are fairly consistent around 100 hours and can be described by a four term exponential that covers both regimes,

$$DC = A_1 e^{-t/32} + A_2 e^{-t/17.2} + A_3 e^{-t/61.5} + A_4 e^{-t/311} + C. \quad (5)$$

The best fit amplitudes to each exponential are found to be  $A_1 = (3.43 \pm 0.001) \times 10^6$ ,  $A_2 = (9.8 \pm 0.1) \times 10^5$ ,  $A_3 = (2.0 \pm 1.3) \times 10^4$ ,  $A_4 = (4.8 \pm 4.1) \times 10^3$ , and  $C = (0.4 \pm 1.1) \times 10^3$ , in units of  $e^-/\text{pixel}/\text{hr}$ . The curve describing this model can also be found in Figure 9. Although the longer time constants are poorly constrained, the values agree quite well with the values from the two term fit to the proton-irradiated data.

The similarity between the dark current in the proton-irradiated CCD and the  $^{60}\text{Co}$ -irradiated CCD indicates that ionizing radiation may be primarily responsible for the generation of dark current. Similar results have been observed in experiments with other p-channel devices [10]. One possible explanation may be that the 0.1 - 1.0 MeV electrons occasionally disrupt the lattice, causing bulk damage and increased dark current without the traps responsible for degraded CTE. To conclusively determine the origins of dark current requires additional irradiation at the  $^{60}\text{Co}$  source with measurements covering a period of several weeks to provide constraints on the longer decay constants and varying the experimental configuration to probe the damage caused by electrons and photons of different energies.

## VIII. DISCUSSION

Both the parallel and serial CTE scale roughly as expected as a function of proton energy, providing evidence that the NIEL approximation of CTE degradation is fairly robust. Previous experiments have indicated that damage factors at higher energies tend to deviate from the NIEL approximation; however the NIEL approximation is still considered the best model of radiation exposure [27]. The NIEL approximation in this case assumes protons as the primary source of radiation damaged and we should add the caveat that the effects of secondary neutrons have not been considered. Assuming the NIEL approximation is valid, we extrapolate the results of the 12.5 MeV irradiation to model the effects of exposure at the L2 Lagrange point.

In estimating the performance of the SNAP CCDs after six years at L2, we consider CTE mitigation by the zodiacal background and cosmic rays in a typical 300 second exposure. Simulations predict a zodiacal background of  $0.166 e^-/\text{s}/\text{pixel}$  around 400 nm and  $0.446 e^-/\text{s}/\text{pixel}$  at 1000 nm for the current filter design [28]. For the purposes of this analysis, we use the lowest level of zodiacal from the bluest filter, or  $49.8 e^-/\text{pixel}$  for a 300 s SNAP exposure. We have also computed the expected cosmic ray contamination for a single SNAP exposure, as shown in Figure 10. As a rough estimate, we assume that trap-filling by  $^{55}\text{Fe}$  x-rays is a fair estimate of trap-filling by cosmic rays above a threshold of  $1600 e^-$ . We therefore use a value of  $2.33 \times 10^{-3}$  events/pixel for determining CTE performance in orbit. Although the results shown in Figure 10 indicate that a fairly large number of pixels will be contaminated by cosmic rays, it should be noted that

the dithering strategy will provide multiple exposures that will be used to reject most cosmic rays.

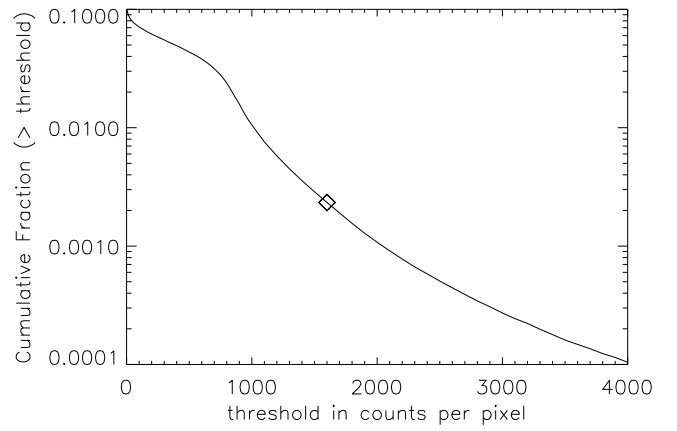


Fig. 10. Expected cumulative distribution of cosmic ray counts per pixel. The symbol at  $1600 e^-$  represents the density of cosmic rays above a threshold corresponding to the average  $^{55}\text{Fe}$  x-ray event.

Extrapolating to the expected displacement damage dose and modeling the mitigation of CTE according to Equation 3, the SNAP CCDs are expected to perform extremely well. Assuming a baseline CTE of 0.999 999 before launch, we calculate a parallel CTE of 0.999 996 after six years. The serial CTE is somewhat better, with a predicted value of 0.999 997 after six years. If the device is never annealed, half the serial CTE degradation will occur.

As argued in §V-F, the SNAP CCDs are quite resilient to hot pixels after irradiation. Hot pixels affect a very small area of the SNAP CCD, only  $1.13 \times 10^{-4}$  for a fluence of  $2 \times 10^{10}$  protons/cm<sup>2</sup> assuming a threshold of 100  $e^-$  in a ten minute exposure. Scaling this result to the displacement damage dose expected, we expect  $4.1 \times 10^{-6}$  of the pixels to be contaminated by dark current spikes in orbit at L2. Considering the  $3512 \times 3512$  layout of the SNAP CCDs, this level of contamination is equivalent to a single column defect only 48 pixels long. The SNAP observing strategy implements a dither pattern to cover gaps between detectors, equivalent to several hundred columns in width. The contribution from both column defects and hot pixels will be minor relative to the spacing between detectors, and the dither pattern will be sufficient to cover any detector area lost due to these defects.

Finally, we interpret the level of dark current following irradiation in the context of the SNAP mission. Ideally, the dominant background in SNAP observations will come from the sky itself, with the dark current generation in the CCDs playing only a minor role. We estimate the expected level of dark current after six years by taking the constant term without annealing, and scaling the damage displacement dose to the predicted levels from SPENVIS. After six years with no anneal, the dark current of  $20 e^-/\text{hr}$  is significantly lower than the minimum level of zodiacal of  $600 e^-/\text{hr}$  around 400 nm. Assuming Poisson statistics, this level of dark current will only increase the RMS contribution from the background by 2% for the bluest filter. The situation improves after an anneal. Dark

current due to radiation exposure is therefore not expected to degrade the sensitivity of SNAP observations of SNe or weak lensing shear.

## IX. CONCLUSION

The behavior of thick, fully depleted, p-channel LBNL CCDs designed for the SNAP satellite has been investigated using irradiation at the LBNL 88-Inch Cyclotron and LBNL  $^{60}\text{Co}$  source. We have performed extensive tests of charge transfer efficiency, generation of dark current, and hot pixel formation from proton exposure. A summary of the results scaled to the expected exposure at L2 can be found in Table VII. CTE performance after irradiation is calculated assuming pre-radiation parallel and serial CTEs of 0.999 999. The radiation studies show that the LBNL CCDs designed for use in the SNAP satellite will develop negligible contamination from dark current and hot pixels during the course of a six year mission.

TABLE VII  
EXPECTED CCD PERFORMANCE AFTER SIX YEARS AT L2

Quantity	Pre-irrad	Nominal Exposure
Defect Pixels	< 0.001	$4.1 \times 10^{-6}$
Dark Current	3 – 4 e <sup>-</sup> /hr	20 e <sup>-</sup> /hr
Ser CTE-no anneal	0.999 999	0.999 998
Ser CTE-w/anneal	0.999 999	0.999 997
Parallel CTE	0.999 999	0.999 996

Monte Carlo simulations by propagation of solar protons through the complex shielding of the SNAP satellite will finalize estimates of radiation exposure over the mission lifetime. Additional analysis is required to quantify the impact of the degraded performance on science observations: CTE degradation impact on galaxy shapes for weak lensing science goals and CTE dependence on sources signal strength. Future studies of the effects of  $^{60}\text{Co}$  irradiation over a longer time span would be useful in better understanding the mechanism for the generation of dark current.

Future irradiation studies are planned to identify the defects responsible for dark current and CTE degradation as briefly mentioned in §V-D. We will identify specific trap locations and densities with pocket pumping. Pocket pumping and CTE measurements with varying temperature and clocking rates will provide estimates of the trap time constants. These measurements will be valuable in quantifying the nature of the traps responsible for the CTE degradation and explaining the transition in the trap populations caused by the anneal to warm temperature.

Nevertheless, the results reported here show that the LBNL CCDs are significantly more radiation tolerant than n-channel CCDs currently in use in space-based observatories. This makes the LBNL CCDs an excellent choice for use in future space-based missions such as SNAP.

## ACKNOWLEDGMENT

The authors would like to acknowledge the contribution of M. Uslenghi in writing software used to compute CTE values generated in this work. In addition, the authors thank C.

Stoughton for his comments on the manuscript and the referees for their contribution in the reviewing process. This work was sponsored by the United States Department of Energy under contract No. DE-AC02-05CH11231.

## REFERENCES

- [1] G. Aldering et al., “Supernova / Acceleration Probe: A Satellite Experiment to Study the Nature of the Dark Energy”, astro-ph/0405232, 2004.
- [2] S. E. Holland, D. E. Groom, N. P. Palaio, R. J. Stover, and M. Wei, “Fully depleted, back-illuminated charge-coupled devices fabricated on high-resistivity silicon,” IEEE Trans. Elec. Dev., 50, 225, 2003.
- [3] S. E. Holland, C. J. Bebek, K. S. Dawson, J. H. Emes, M. H. Fabricius, J. A. Fairfield, D. E. Groom, A. Karcher, W. F. Kolbe, N. P. Palaio, N. A. Roe, and G. Wang, “High-voltage-compatible, fully depleted CCD development”, SPIE, 6276, 10H, 2006.
- [4] D. E. Groom, C. J. Bebek, M. Fabricius, A. Karcher, W. F. Kolbe, N. A. Roe, and J. Steckert, “Quantum efficiency characterization of back-illuminated CCDs Part 1: The Quantum Efficiency Machine,”, SPIE, 6068, 2006.
- [5] M. H. Fabricius, C. J. Bebek, D. E. Groom, A. Karcher, and N. A. Roe, “Quantum efficiency characterization of back-illuminated CCDs Part 2: Reflectivity measurements”, SPIE, 6068, 2006.
- [6] J. Janesick, G. Soli, T. Elliot, and S. Collins, “The effects of proton damage on charge-coupled devices”, Charge-Coupled Devices and Solid State Optical Sensors II, SPIE, 1447, 87, 1991.
- [7] J. R. Srour and D. H. Lo, “Universal Damage Factor for Radiation-Induced Dark Current in Silicon Devices”, IEEE Trans. Nucl. Sci., 47, 2451, 2000.
- [8] J. R. Srour, C. J. Marshall, and P. W. Marshall, “Review of Displacement Damage Effects in Silicon Devices”, IEEE Trans. Nucl. Sci., 50, 653, 2003.
- [9] J.P. Spratt, C. Conger, R. Bredthauer, W. Byers, R. Groulx, R. Leadon, and H. Clark, “Proton damage effects in high performance p-channel CCDs,” IEEE Trans. Nucl. Sci., 52, 2695, Dec. 2005.
- [10] J.P. Spratt, B. C. Passenheim, R. E. Leadon, “The Effects of Nuclear Radiation on p-channel CCD Imagers,” in 1997 IEEE Radiation Effects Data Workshop, NSREC Snowmass.
- [11] G.R. Hopkinson, “Proton Damage Effects on p-channel CCDs,” IEEE Trans. Nucl. Sci. 46(6), pp.1790-1796, 1999.
- [12] C. Marshall, P. W. Marshall, A. Waczynski, E. Polidan, S. J. Johnson, and H. Campbell, “Comparisons of the proton-induced dark current and charge transfer efficiency responses of n- and p-channel CCDs”, SPIE, 5499, 542, 2004.
- [13] C. J. Bebek, D. E. Groom, S. E. Holland, A. Karcher, W. F. Kolbe, M. E. Levi, N. P. Palaio, B. T. Turko, M. C. Uslenghi, M. T. Wagner, and G. Wang, “Proton radiation damage in high-resistivity n-type silicon CCDs”, SPIE 4669, 161-171, 2002.
- [14] M. A. Xapsos, J. L. Barth, E. G. Stassinopoulos, E. A. Burke and G. B. Gee, “Space Environment Effects Model for Emission of Solar Protons (ESP) Cumulative and Worst Case Event Fluences”, NASA/TP-1999-209763, 1999.
- [15] <http://www.spennis.oma.be>
- [16] I. Jun, M. A. Xapsos, S. R. Messenger, E. A. Burke, R. J. Walters, G. P. Summers, and T. Jordan, “Proton nonionizing energy loss (NIEL) for device applications”, NSS-IEEE, 50, 1924, 2003.
- [17] A. Schenk, “A Model for the Field and Temperature Dependence of Shockley-Read-Hall Lifetime in Silicon”, Solid-State Elec., 35, 1585, 1992.
- [18] M. Tsuchiaki, H. Fujimori, T. Inuma, A. Kawasaki, “An Interface State Mediated Junction Leakage Mechanism Induced by a Single Polyhedral Oxide Precipitate in Silicon Diode”, Journal of Applied Physics, 85, 8255, 1999.
- [19] S. E. Holland, K. S. Dawson, N. P. Palaio, J. Saha, N. A. Roe, and G. Wang, “Fabrication of Back-Illuminated, Fully Depleted Charge Coupled Devices”, Nuclear Instruments and Methods, 5, 265, 2007.
- [20] T. Hardy, R. Murokowski, and M. J. Deen, “Charge Transfer Efficiency in Proton Damaged CCD’s”, IEEE Trans. Nucl. Sci., 45, 154, 1998.
- [21] M. Sirianni, M. J. Jee, N. Bentez, J. P. Blakeslee, A. R. Martel, G. Meurer, M. Clampin, G. De Marchi, H. C. Ford, R. Gilliland, G. F. Hartig, G. D. Illingworth, J. Mack, and W. J. McCann, “The Photometric Performance and Calibration of the Hubble Space Telescope Advanced Camera for Surveys,” Publications of the Astronomical Society of the Pacific, 117, 836, 1049-1112, 2005.

- [22] M. Bautz, G. Prigozhin, S. Kissel, B. LaMarr, C. Grant, and S. Brown, "Anomalous annealing of a high-resistivity CCD irradiated at low temperature", *NSS-IEEE*, 52, 519, 2005.
- [23] J.Janesick, "Scientific Charge-Coupled Devices," SPIE Press, 2001.
- [24] A.Riess and J.Mack, "Time Dependence of ACS WFC CTE Corrections for Photometry and Future Predictions," Instrument Science Report ACS 2004-006, 2004.
- [25] E. J. Polidan, A. Waczynski, P. W. Marshall, S. J. Johnson, C. Marshall, R. Reed, R. A. Kimble, G. Delo, D. Schlossberg, A. M. Russell, T. Beck, Y. Wen, J. Yagelowich, R. J. Hill, and E. Wassell, "A study of hot pixel annealing in the Hubble Space Telescope Wide Field Camera 3 CCDs", *SPIE*, 5167, 258, 2004.
- [26] M. Sirianni, M. Mutchler, M. Clampin, H. C. Ford, G. D. Illingworth, G. F. Hartig, D. van Orsow and T. Wheeler, "Performance of the Advanced Camera for Surveys CCDs after two years on orbit", *SPIE*, 5499, 173, 2004.
- [27] C. Dale, P. Marshall, B. Cummings, L. Shamey, A. Holland, "Displacement Damage Effects in Mixed Particle Environments for Shielded Spacecraft CCDs", *IEEE Trans. Nucl. Sci.*, 40, 1628, Dec. 1993.
- [28] T. M. Davis, B. P. Schmidt, and A. G. Kim, "Ideal Bandpasses for Type Ia Supernova Cosmology", *Publications of the Astronomical Society of the Pacific*, 118, 205, 2006.